The impact of temperature on heated liquid films: Crater and jetting impact dynamics

Daniel A. Vasconcelos [*], André R.R. Silva, Jorge M.M. Barata

AEROG - Aeronautics and Astronautics Research Center, LAETA, University of Beira Interior, Covilhã, Portugal

ARTICLE INFO

ABSTRACT

The droplet impact phenomena onto liquid films are a field extensively researched for over a century, which are driven by many practical applications such as heat exchangers, internal combustion engines and spray cooling. Despite the extensive work on wetted surfaces, the influence of temperature on droplet outcome, local evaporation/boiling effects, and liquid film stability has been overlooked in the literature. Therefore, the main objective of this work is to evaluate the influence of the liquid film temperature on the crater and jet dynamics. The experimental setup was designed for this purpose, in which a borosilicate glass surface that contains the liquid film is placed over an aluminium block with embedded cartridge heaters, heating it by conduction. Water, n-decane and n-heptane are the fluids adopted for the experiments due to their differences in thermophysical properties and saturation temperature. Different conditions are considered, which include two dimensionless thicknesses, $h^* = 1.0$ and $h^* = 1.5$, and a range of dimensionless temperatures, $\theta = 0$, $\theta = 0.2$, $\theta = 0.4$ and $\theta = 0.6$. Qualitative and quantitative analyses are performed regarding crater evolution, and central jet height and breakup measurements, respectively. Evaporation rate measurements are required due to the influence on the liquid film thickness variation. Qualitative results show that temperature differences promote the formation of recirculation zones near the impact surface and the crater boundaries, as well as the influence on the crater shape and curvature. In terms of the quantitative analysis, the central jet height measurements for the n-heptane and n-decane reveal that higher values of the dimensionless temperature lead to an increase in the jet height, as well as promoting and increasing the occurrence and number of secondary droplets, respectively. Water follows a similar trend with the exception of $\theta = 0.2$, which can be explained by a time scale analysis.

1. Background

The droplet impact phenomena has been an interesting field for over a century. The early pioneer work of Worthington [1] led to a multitude of studies, described by several authors [2–4], which involve interfacial phenomena, such as surface tension, evaporation and condensation, surface morphology [5], two-phase flow dynamics [6,7], combustion [8,9], among others. Nowadays, research on this topic is mainly driven by industrial applications, such as heat exchangers [10], internal combustion engines [11], spray cooling [12], ink-jet printing [13], etc.

There are several dimensionless numbers that define the droplet impact phenomena. The Weber number represents the ratio of disruptive hydrodynamic to the stabilising surface tension forces, $We = \rho U_0^2 D_0/\sigma$, where ρ is the fluid density, U_0 is the droplet impact velocity, D_0 is the droplet diameter, and σ is the surface tension. The Reynolds number relates the inertial to the viscous forces, $Re = \rho U_0 D_0/\mu$, where μ is the

fluid viscosity. The Froude Number, $Fr = U_0^2/gD_0$, relates the inertial to the gravitational forces, where g is the gravitational acceleration constant. The Ohnesorge number, $Oh = \mu/\sqrt{\rho\sigma D_0}$, is defined as the ratio between the viscous forces and the inertial and surface tension forces. The different combinations of the inertial and thermophysical properties lead to a variety of outcomes, which includes deposition, prompt and corona splash, central jet, among others [14].

The study of crater formation has been previously researched, as described by the review of Prosperetti and Oguz [15]. Work performed prior to this point focused on the mechanics of rain underwater noise, which is linked to acoustical phenomena. In terms of crater dynamics, these can be entirely described by the Weber and Froude number, as the influence of viscosity is considered negligible [16]. The crater shape is dependent on the liquid film thickness, ranging from hemispherical for deep pools to oblate for liquid films. This occurs due to the constraint

---

Nomenclature

$\dot{h}$	Liquid film thickness evaporation rate [mm/s]
D_0	Droplet impact diameter [mm]
D_c	Borosilicate glass cylinder inner diameter [cm]
e_c	Borosilicate glass cylinder thickness [cm]
Fr	Froude Number [−]
g	Gravitational acceleration constant [m/s^2]
h	Liquid film thickness [mm]
h^*	Dimensionless liquid film thickness [−]
H_{jet}^*	Dimensionless central jet height [−]
H_{jet}	Central jet height [mm]
N	Total number of observations [−]
n_b	Number of central jet breakups [−]
Oh	Ohnesorge Number [−]
q	Heat flux [W/m^2]
Re	Reynolds Number [−]
T	Temperature [°C]
t	Time [s]
U_0	Droplet impact velocity [m/s]
We	Weber Number [−]
x_i	Experimental values [−]

Greek Symbols

α	Thermal diffusivity [m^2/s]
μ	Dynamic viscosity [mPa/s]
μ_{st}	Average value [−]
ν	Kinematic viscosity [m^2/s]
ρ	Density [kg/m^3]
σ	Surface tension [mN/m]
σ_{st}	Standard deviation [−]
τ	Dimensionless time [−]
θ	Dimensionless temperature [−]

Subscripts

air	Surrounding air
conv	Related to convective effects
drop	Droplet
f	Liquid film
grav	Related to gravitational effects
sat	Saturation point
therm	Related to thermal effects
vis	Related to viscous effects

that both the wall and the liquid film impose on the crater development. These craters may transition to a conical shape if a capillary wave forms after impact and propagates along the crater wall [17]. Berberović et al. [17] evaluated the crown formation for different liquid film thicknesses, $0.5 < h^* < 2$, impact velocities, and fluids. The cavity depth measurements display similar tendencies for early impact stages and are posteriorly conditioned by the liquid film thickness, whereas an increase in the Weber number and a decrease in the film thickness leads to higher crater diameters. Bisighini et al. [16] analysed the crater characteristics for deep pool droplet impact for $170 < We < 2190$ and $262 < Fo < 694$. The measurements show that increasing values of Weber and Froude numbers lead to a higher maximum crater depth and correspondent time. Most recently, experimental work involving crater analysis focuses on burning liquid films [18,19], several liquid layers [20] or different fluids for droplet and liquid film [21,22], which underlying dynamics are fundamentally different.

Succeeding the maximum crater expansion, there is a retraction period. This process can lead to the formation of a Rayleigh/central jet, with or without breakup, or crown splashing, which are dependent on the balance between the inertial, viscous and surface tension forces [23]. The spatial evolution of the Rayleigh jet involves specific dynamics, such as pinch-off [24] and secondary atomisation associated with height development. The pinch-off location shifts from a lower to an upper position when subjected to higher accelerations [25]. In terms of jet development and consequent breakup, the maximum jet height does not follow a linear tendency with the Weber number, which tends to display more disparate values for higher Weber numbers. The time at which the central jet reaches the maximum height has an improved trend in comparison with the central jet measurements. An increase in the Weber number leads to a later time the central jet reaches a maximum [26]. Castillo et al. [23] developed regime maps for Rayleigh jet breakup on deep pools, distinguishing no breakup, Rayleigh jet breakup and crown splash based on the Weber, Reynolds and Ohnesorge numbers. Higher impact velocities lead to an increase in the central jet height. For Weber numbers below the critical value, no breakup occurs. This value increases for higher Ohnesorge numbers, as the crown instabilities are dampened due to the increase of viscosity. The central jet breakup is suppressed for $Oh > 0.091$, as the outcome transitions directly from no breakup to crown splashing with the increase of the Weber number. Manzello et al. [27] studied the impact of water droplets onto liquid films, varying the Weber number and liquid film thickness, ranging from $We = 5.5$ to $We = 206$, and from $h^* = 0.6$ to $h^* = 8.1$, respectively. The authors concluded that the critical Weber number is independent of the liquid film thickness. However, no jet breakup was verified for the lower thicknesses, $h^* = 0.6$ and $h^* = 1.3$, in comparison to deep pool regimes, meaning that liquid film thicknesses considerably higher than the droplet diameter promote the occurrence of jet breakup. The jet height measurements display maximum values for $h^* = 1.3$. However, increasing the liquid film thickness beyond this value leads to a reduction in the maximum jet height, which is more significant for $We = 206$.

The fluid viscosity also exhibits a role in the jet evolution. Michon et al. [28] stated that the central jet grows faster with the increase of liquid viscosity up to $\mu = 6$ mPa s, which is contrary to the popular belief that an increase in viscosity leads to the underdevelopment of the velocity fields. This occurs due to the cavity not being disturbed by capillary waves, smoothing its collapse and leading to faster and thinner jets that emerge from the impact region [29]. For higher viscosities, up to $\mu = 15$ mPa s, bubble entrapment and high-speed jets are suppressed and, for $Fr \geq 300$, the jet emerging velocity is independent of the liquid viscosity. Ghabache [29] studied the relation between a crater formed by the release of a gas bubble in the liquid, and the upcoming jet from the bursting bubble. The results show that the jet velocity is inversely proportional to the radius of the bubble. For $\mu < 6$ mPa s, for the studied range of bubble radius, the jet velocity increases for higher values of viscosity.

In modern applications, such as internal combustion engines, promoting secondary atomisation originated from droplet impact onto liquid films is crucial to improve the fuel/air mixture preparation and, consequently, the combustion efficiency. Different parameters of the droplet, the liquid film and the surrounding gas are factors that determine the outcome of the impact and, due to this, understanding jetting, among other sources of atomisation, is essential. Despite the extensive work on liquid films, the influence of temperature on droplet outcome, local evaporation/boiling effects, and liquid film stability has been overlooked in the literature [4]. Most recently, several authors have been researching heated liquid films regarding fire suppression [22,30, 31], characterised by water–oil interactions and immiscible properties of the droplet and the liquid film. Even though one could correlate to different applications, there are inherent phenomena that arise due to the interaction of different fluids, such as vapour plume bursting and explosion.

Table 1
Thermophysical properties of water, n-decane and n-heptane at room temperature ($T = 20$ °C).

Fluid	ρ [kg/m³]	μ [mPa s]	σ [mN/m]	T_{sat} [°C]
Water	998.2	1.002	72.73	99.8
N-heptane	685.8	0.412	20.29	98.4
N-decane	732.1	0.929	23.89	174.1

Therefore, the main objective of the current work is to evaluate the influence of the liquid film temperature on the crater and jet dynamics, and to visualise the occurrence of temperature-related phenomena. Qualitative and quantitative analyses are performed regarding crater evolution, and central jet height and breakup measurements, respectively.

2. Experimental setup

The experimental setup is illustrated in Fig. 1. It consists of five main components, including the pumping system, the image acquisition, the heating controller device, the illumination source and the impact surface. A droplet is formed at the tip of a hypodermic needle through a NE-1000 syringe pump that pushes the fluid through a tube that is connected to the needle. The droplet is allowed to free-fall under the influence of gravity. The droplet impacts onto a stationary liquid film confined by a two-part borosilicate glass container. This container comprises of a borosilicate glass hollow cylinder with an internal diameter of $D_c = 12$ cm and a thickness of $e_c = 0.5$ cm, coupled to a borosilicate glass plate of 15 cm × 15 cm × 0.2 cm. The distance between the droplet impact region and the boundaries of the container is ≈ 20 times higher than the largest droplet diameter, meaning that the liquid film thickness is considered uniform throughout the surface, and the boundaries of the container do not influence the droplet impact phenomenon [23,32,33]. To guarantee that there is no fluid leaking through the contact area of both parts, these are glued by an acetoxy silicone, LOCTITE® SI 5366, which is a bonding agent specifically designed for sealing up to operating temperatures of $T = 250$ °C. In order to heat the liquid film, the borosilicate glass container is placed on an aluminium block of dimensions 15 cm × 15 cm × 3 cm with four embedded cartridge heaters of 250 W each. Each heater has a length of 12.5 cm and is fixated laterally into the aluminium block, heating it by conduction and, consequently, the liquid film. The surface temperature is controlled by a heating device connected to an embedded K-type thermocouple 0.75 cm below the aluminium surface. A graphite plate of 15 cm × 15 cm × 0.4 cm is positioned amidst the aluminium block and the glass surface to block reflections from the aluminium. In terms of image acquisition, a high-speed camera was employed for the droplet impact phenomena visualisation. A Photron FASTCAM mini UX50 with a Macro Lens Tokina AT-X M100 AF PRO D was used at a frame rate of 4000 fps for a resolution of 1250 × 512 pixels. The shutter was varied between 20000–40000 fps for the experiments, requiring higher shutter values for higher temperatures and liquid film thicknesses. The illumination source was provided by a LED lamp and positioned opposite to the high-speed camera, combined with a diffusion glass in between for uniform lighting. A precision scale is adopted to verify the liquid film thickness by weight and the evaporation rate measurements, which will be detailed in the following section. The precision scale is positioned on the side and not under the aluminium block, as the representation in Fig. 1 is solely for visualisation purposes.

The fluids adopted for the experiments are water, n-decane and n-heptane. These were selected due to the differences in thermophysical properties and saturation temperature, which are displayed in Table 1. In addition, water is a reference fluid extensively researched [34], and the n-decane and n-heptane are surrogate fuels for kerosene/jet-fuel [35,36] and diesel [37,38], respectively.

Fig. 2 displays the schematic of the physical setup. A single droplet, of diameter D_0 and impact velocity U_0, free falls vertically until impacting a liquid film of thickness h. The droplet is considered at room temperature, $T_{drop} = T_{air}$, and the liquid film is heated by a heat flux, q, generated in the aluminium block by the cartridge heaters until reaching a specific temperature, T_f. The dimensionless temperature, $\theta = (T_f - T_{air}) / (T_{sat} - T_{air})$, correlates the saturation temperature of the fluid, T_{sat}, the temperature of the liquid film and the temperature of the surrounding air. Therefore, the dimensionless temperature varies between $\theta = 0$ and $\theta = 1$, where $\theta = 0$ corresponds to the liquid film and the droplet at room temperature, $T_f = T_{drop} = T_{air}$, and $\theta = 1$ to the liquid film at saturation temperature, $T_f = T_{sat}$.

Fig. 3 displays a flowchart for the droplet impact onto heated liquid films (for $\theta > 0$). With the aid of a high-speed digital camera, the droplet impact is recorded, and the droplet physical parameters, namely its diameter and impact velocity, are analysed through MATLAB. The algorithm processes the images obtained through binarisation and detection of contiguous regions. Initially, background subtraction is performed to differentiate the droplet from its surroundings. The processed image is then binarised through the Otsu's method [39], and the properties of the droplet are measured, consisting on its horizontal and vertical diameters, and centroid, for a substantial number of frames. The droplet diameter is calculated by averaging the horizontal and vertical diameters during free fall. In contrast, the impact velocity is defined by the difference of centroids of the last frame before impact and successive prior frames. The dimensionless numbers, such as the Reynolds and Weber numbers, are calculated based on this analysis. Due to the dependency of the droplet diameter on the dimensionless film thickness, the evaporation rate and liquid film temperature measurements are performed subsequent to the droplet analysis, which will be presented more thoroughly in the following section. Once these are fully characterised, the liquid film is then heated for an extended period of time until reaching a stabilisation temperature. However, due to evaporation, the liquid film thickness initially established changes over time. Therefore, the liquid film must be re-evaluated by being weighted with a precision scale. If the liquid film weight is over an acceptable range (meaning there is an excess in fluid), then fluid should be removed, either manually by means of a syringe or through evaporation over a period of time, as mentioned in Fig. 3, until reaching a certain liquid film weight and, correspondingly, thickness. If, due to excess evaporation, the liquid film thickness has decreased, then fluid should be added to the liquid film, followed by a period of temperature stabilisation. This iterative process is concluded once the weight of the liquid film is within a confidence interval of 95%. Once all of these conditions are met, the droplet is released from the tip of the needle, impacting the heated liquid film. Different authors range their experiments from 3 to 5 impacting droplets for isothermal conditions [23,27,40,41]. Due to the influence of temperature on the liquid film and impact phenomena, and following previous works [7,42], a minimum of 10 impacting droplets is considered for each experimental condition to ensure repeatability and consistency of the results. Pixel size was varied between 29.8 μm and 38.7 μm. Posteriorly, the post-processing of the results is performed, such as visualisation, analysis of the central jet, and the overall influence of temperature. The average, μ_{st}, and standard deviation, σ_{st}, measurements are calculated by the following equations, $\mu_{st} = \sum_{i=1}^{N} x_i / N$ and $\sigma_{st} = \sqrt{\sum_{i=1}^{N} (x_i - \mu_{st}) / N}$, respectively, where x_i are experimental values and N is the total number of observations. The experimental measurements, including the droplet parameters, liquid film temperature and evaporation rate, and central jet height, were calculated based on these statistical functions. The jet height measurements were performed through a MATLAB algorithm. Similarly to the droplet analysis, a background subtraction and binarisation were required to highlight the impact region and the central jet. Image cropping was performed on the liquid film interface in order to isolate the central jet and to minimise possible measurement errors. Subsequently, a filtering function was applied to remove any additional noise, followed by the height measurements on the region of interest.
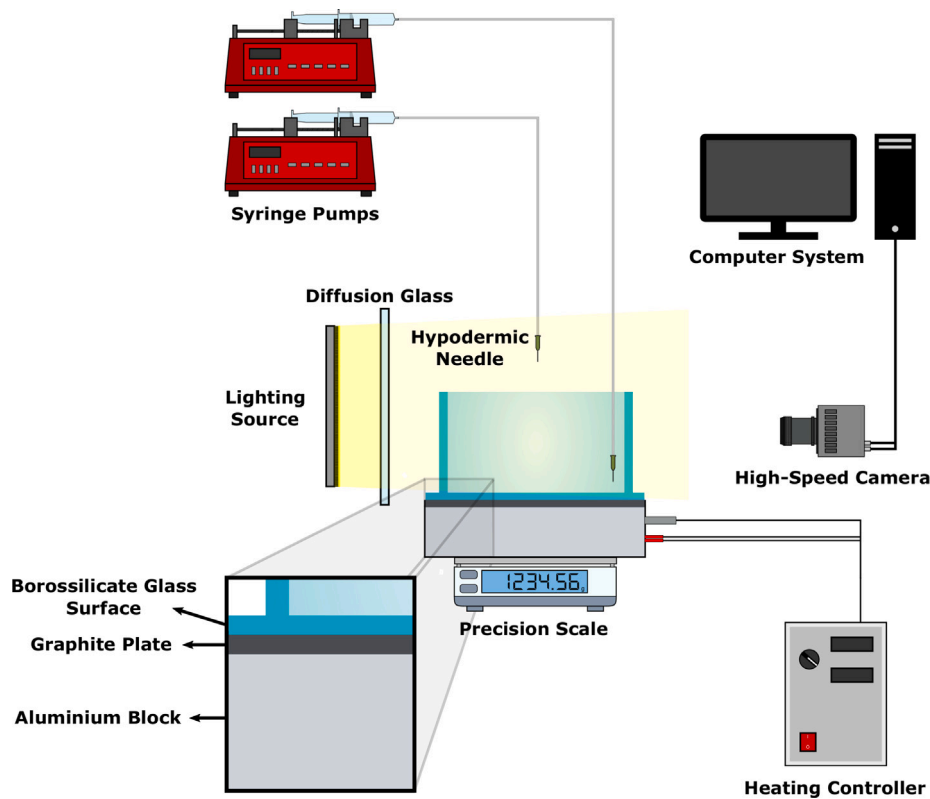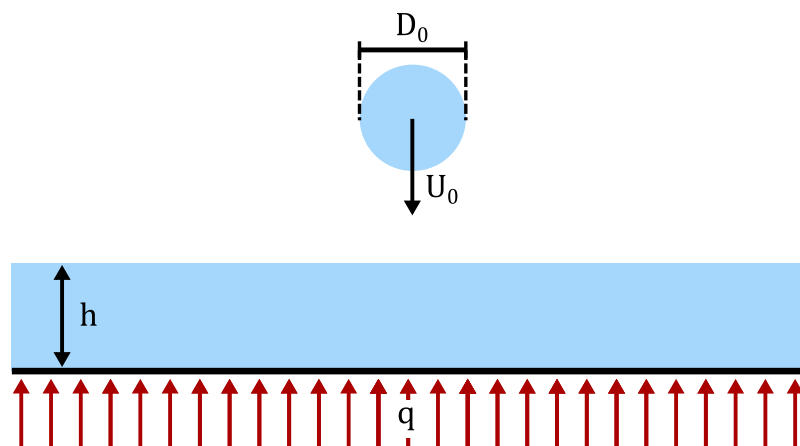
Fig. 1. Schematic of the experimental setup.

Fig. 2. Schematic of a droplet impinging onto a liquid film affected by a heat flux.

3. Results and discussion

Prior to studying the droplet impact phenomena, we must verify the conditions regarding the surrounding air and the droplet/liquid film. Air temperature and humidity were kept at 20 ± 2 °C and $50 \pm 3\%$, respectively. As a temperature is selected by the heating device, the cartridge heaters act as a heat source, consequently heating the liquid film. However, due to heat dissipation between the liquid film and the surrounding environment, its temperature is expected to be lower than the previously selected temperature. Therefore, the temperature measurements of the liquid film are crucial not only to define the impact phenomena, but also for the corresponding evaporation measurements that will follow. Due to this, six K-type immersion thermocouples were coupled to a height gauge with micrometre precision for the liquid film temperature measurements. Fig. 4(a) exhibits the thermocouples

placement in the liquid film. The thermocouple probe positioned in the impact region is displayed by the blue cross, represented by P_1. The red crosses, which refer to the remaining thermocouples, are oriented both straight (P_4, P_5 and P_6) and radially (P_2, P_3 and P_4). This orientation allows for temperature measurements at different positions in the liquid film in order to verify its thermal homogeneity. Fig. 4(b) displays how to immerse the thermocouples in the liquid film. The measurements were performed at a vertical distance of 0.1 ± 0.05 mm from the borosilicate glass surface.

Fig. 5 exhibits the n-heptane liquid film temperature measurements for a selected input temperature on the heating device of $T = 70$ °C. The measurements were performed for approximately 30 min after reaching a stability state. For this particular case, the liquid film reaches a temperature of $T_f = 66.5$ °C, which is slightly lower than the one established on the heating device. The temperature measurements were performed for several ranges and fluids, and show a similar tendency to
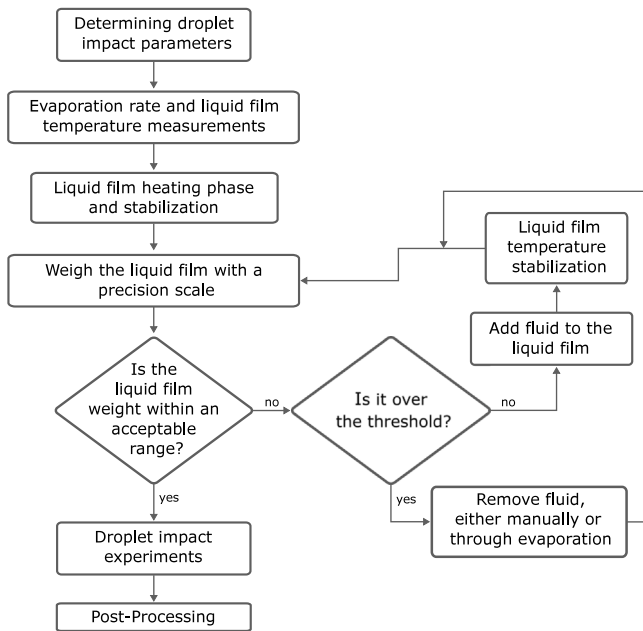
Fig. 3. Flowchart of the experimental procedure.

Table 2
Impact parameters and dimensionless numbers of the study cases for different fluids.

Fluid	D_0 [mm]	U_0 [m/s]	We	Re	Fr
Water	2.67 ± 0.04	2.71 ± 0.01	269	7208	280
N-heptane	2.56 ± 0.06	1.75 ± 0.01	265	7450	122
N-decane	2.72 ± 0.07	1.80 ± 0.01	270	3856	121

range of dimensionless temperatures, $\theta = 0$, $\theta = 0.2$, $\theta = 0.4$ and $\theta = 0.6$.

Figs. 7a and 7b show the influence of θ on the crater overall development for both water and n-decane at different impact conditions. It is possible to visualise the existence of temperature-related dynamics near the crater and the impact surface. These are denominated as recirculation zones, and are promoted by increasing values of θ. At $\theta = 0$, meaning that the droplet and the liquid film are at ambient temperature, water and n-decane do not display recirculation zones. However, for $\theta > 0$, due to the temperature differences, these regions near the crater boundaries begin to emerge, which are properly captured with the high-speed digital camera. In terms of crater shape, for water, temperature also affects its growth, altering its local curvature near the impact surface. For the n-decane, there is a slight shift in crater shape, transitioning from an oblate ($\theta = 0$ and $\theta = 0.2$) to a conical shape ($\theta = 0.4$ and $\theta = 0.6$). These may occur due to the maximum crater diameter being influenced by the liquid temperature, leading to differences in its formation. The crater should be analysed quantitatively in future studies in order to correlate with the jet formation regarding maximum diameter and depth as a function of the liquid film temperature.

Succeeding the qualitative analysis regarding crater formation and retraction, the central jet parameters, such as its height and breakup, are quantified. Fig. 8 represents the growth of the central jet and possible breakup, inducing secondary atomisation. The height of the jet, H_{jet}, is defined as the vertical distance from the gas–liquid interface to the top of the jet. If there is a detachment of a secondary droplet from the main central jet, breakup occurs, leading to a sudden decrease of its height and to the formation of secondary atomisation.

Fig. 9 displays the measurements of the ratio of the central jet height to the droplet diameter, $H_{jet}^* = H_{jet}/D_0$, as a function of dimensionless time, $\tau = tU_0/D_0$, for the n-heptane droplet impact. Fig. 9(a) refers to the lower liquid film thickness, $h^* = 1.0$, and Fig. 9(b) to the higher thickness, $h^* = 1.5$. For the lower thickness, the jet height measurements display similar tendencies for the lower temperatures, $\theta = 0$ and $\theta = 0.2$, and no central jet breakup is visualised. The curves follow a continuous path, starting from the emerging central jet, reaching its maximum height, followed by a gradual decrease until merging with the film. However, for higher temperatures, $\theta = 0.4$ and $\theta = 0.6$, there is a clear difference in the jet height, showing higher measurements for increasing values of θ. The maximum jet height also occurs at later stages of impact for higher temperatures, and the impact phenomena occur for longer periods of time. Additionally, it is also possible to verify that, for $\theta = 0.4$ and $\theta = 0.6$, the curves display irregularities opposite to the smoothness at lower temperatures. These can be denominated as line discontinuities, which are associated with secondary atomisation that cause a sudden decrease in the central jet height. For the higher liquid film thickness, the increase of θ promotes higher central jets. Contrary to the lower liquid film thickness, in which $\theta = 0$ and $\theta = 0.2$ exhibited similar results, for this case, ranging from $\theta = 0$ to $\theta = 0.6$, there is a progressive increase of the jet height measurements. Similarly to Fig. 9(a), the duration of the phenomena is also affected by the liquid film temperature. In terms of breakup, there are considerably more discontinuities compared to the lower thickness, meaning that there is more than one jet breakup occurrence throughout the phenomena. Fig. 10 displays the formation and breakup of the central jet for the higher liquid film thickness and $\theta = 0$. It is possible to identify several instances in which the central jet leads to secondary atomisation. The first breakup occurs during the formation
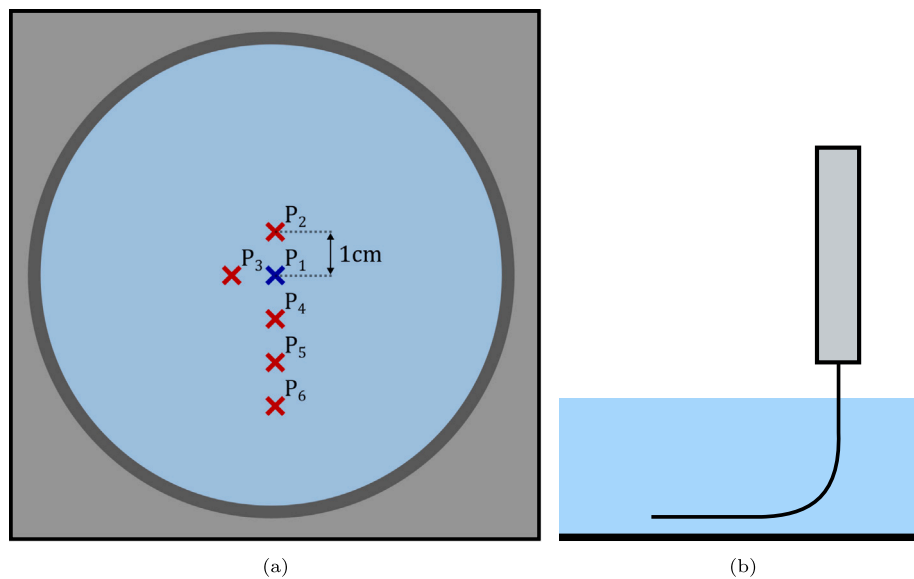
Fig. 5, which includes an initial heating phase until reaching a stability temperature.

As previously stated, subsequent to the analysis of temperature fields, due to evaporation, the liquid film thickness variation must be quantified to guarantee a constant film thickness throughout the experimental study. Fig. 6 displays the liquid film evaporation rate of water, n-heptane and n-decane as a function of the liquid film temperature. The results are presented in mm/min due to the existence of a liquid surface whose thickness varies over time. To measure the evaporation rate, a precision scale with a 0.01 g measurement precision was employed to weigh the liquid film over extended periods of time. The liquid film evaporation rate is represented by $\dot{h}$ due to the nature of the phenomena. The water and n-heptane display higher evaporation rates due to a lower saturation temperature in comparison with n-decane. To guarantee a constant liquid film thickness, a second syringe pump with a pumping rate equal to the evaporation rate is used to add fluid onto the outer region of the borosilicate glass surface. The maximum relative error associated with the temperature measurements is 3.12% for water, 0.45% for n-heptane and 0.43% for n-decane. The maximum relative error for the evaporation rate measurements is 1.34% for water, 0.59% for n-heptane and 1.2% for n-decane.

Upon verifying the conditions regarding the droplet and the liquid film, the study of the droplet impact is initiated. In order to evaluate the influence of the liquid film temperature on the droplet impact outcome, this work focuses on both qualitative and quantitative results. Qualitative analysis is performed on crater evolution, whereas the quantitative data regards to the central jet height and breakup measurements for different liquid film temperatures and thicknesses. The dimensionless temperature, $\theta = (T_f - T_{air})/(T_{sat} - T_{air})$, correlates the saturation temperature of the fluid, T_{sat}, the temperature of the liquid film, T_f, and the temperature of the surrounding air, T_{air}. This parameter is adopted for the current work, which quantifies the influence of temperature on the impact phenomena. Table 2 displays the droplet impact parameters, such as the diameter and impact velocity, which are required to calculate the dimensionless numbers. In order to have similar Weber numbers, due to the water higher surface tension in comparison to the n-decane and n-heptane, the water droplet requires a higher impact velocity. Different conditions are considered, which include two dimensionless thicknesses, $h^* = 1.0$ and $h^* = 1.5$, and a

Fig. 4. Thermocouple positioning on the liquid film. P_1 refers to the position of the first thermocouple, P_2 to the position of the second thermocouple, and so forth: (a) Thermocouple displacement in the liquid film; (b) Visual representation of the immersed thermocouple.
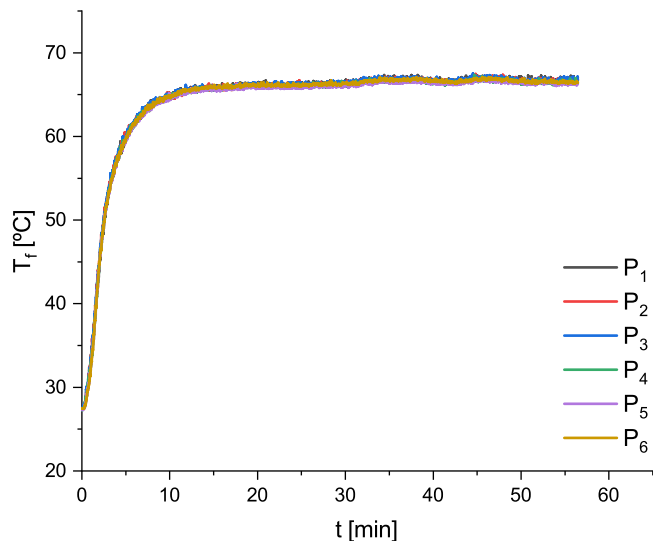

Fig. 5. Liquid film temperature measurements of n-heptane for a selected temperature of $T = 70$ °C on the heating device.
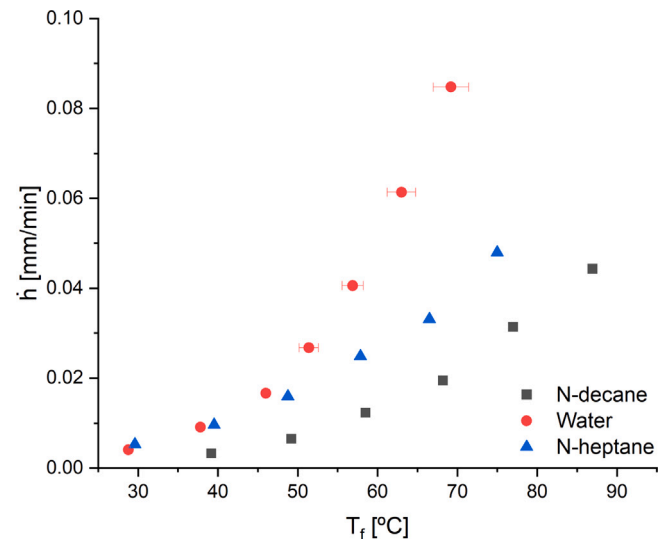

Fig. 6. Evaporation rate of n-decane, water and n-heptane for different liquid film temperatures.

of the central jet, at $\tau = 29.4$, and the jet maintains its growth after the detachment of the secondary droplet. The following breakup occurs at later stages, $\tau = 43.4$, during the descent of the central jet. These can be verified by the line discontinuities in Fig. 9(b). In order to quantify how the dimensionless temperature affects the promotion of the jet breakup, as well as the number of central jet breakups, n_b, associated with the jet growth, Fig. 11 shows the percentages regarding the number of breakups of the central jet as a function of θ. As previously mentioned, a minimum of 10 droplets are considered for each impact condition to ensure repeatability and consistency of the experimental data. For the lower thickness, Fig. 11(a), $\theta = 0$ and $\theta = 0.2$ display $n_b = 0$, meaning that there is no central jet breakup. However, for $\theta = 0.4$, there are 80% of occurrences where no breakup occurs, and 20% in which the central jet breaks one time. For the higher temperature, $\theta = 0.6$, all the jets were affected by breakup, as there is a 100% occurrence on the jet producing one secondary droplet. For Fig. 11(b), the central jet displays breakup tendencies for the entire range of temperatures.

Similar to the previous case, there is a shift in the breakup occurrence percentage. The jet breaks twice $(n_b = 2)$ for $\theta = 0$ and $\theta = 0.2$, with a 100% occurrence for both cases. When increasing the temperature up to $\theta = 0.4$, the central jet breaks 2 to 3 times with an 80%/20% occurrence, respectively. For the highest temperature, $\theta = 0.6$, all the jets formed subsequent to droplet impact led to the formation of 3 secondary droplets. The results presented on the n-heptane droplet impact for the various impact conditions show that higher temperatures not only promote central jet breakup, as well as increase the number of secondary droplets produced.

The central jet height measurements and correspondent breakup for the n-decane droplet impact are presented in Figs. 12 and 13, respectively. For both liquid film thicknesses, Figs. 12(a) and 12(b), higher temperatures lead to an increase in jet height, as well as the duration of the phenomena. This is analogous to the n-heptane, as both fluids follow a similar tendency. In terms of breakup, it is also possible to identify line discontinuities on both cases, which is predominant
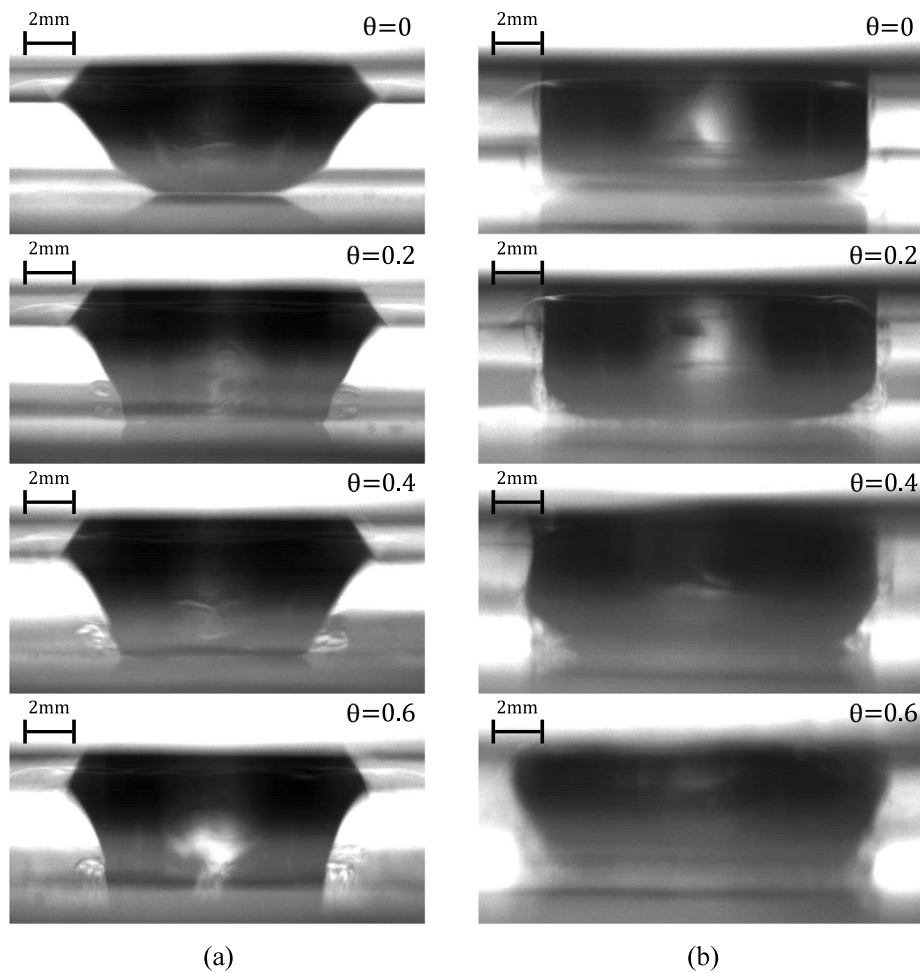
Fig. 7. Visualisation of the crater formation subsequent to droplet impact as a function of dimensionless temperature: (a) Water, $h^* = 1.5$, $\tau = 21.1$; (b) N-decane, $h^* = 1.0$, $\tau = 12.4$.
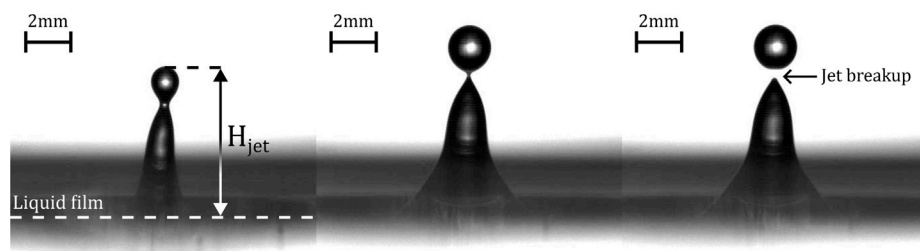

Fig. 8. Representation of the central jet height and posterior breakup.

with central jet breakup. For $h^* = 1.0$, this occurrence can be mainly found for $\theta = 0.4$ and $\theta = 0.6$, whereas for the higher thickness, $h^* = 1.5$, breakup is noticeable for all the temperatures. The number of jet breakups is displayed for both thicknesses in Figs. 13(a) and 13(b). For the lower thickness, $h^* = 1.0$, the central jet does not break at room temperature, $\theta = 0$, displaying a 100% occurrence of no formation of secondary droplets ($n_b = 0$). By increasing temperature, the central jet starts to break, having a 10% chance of breaking once ($n_b = 1$) for $\theta = 0.2$ and, for the higher temperatures, there is a clear transition in the breakup event, as there is a 60% occurrence for one secondary droplet for $\theta = 0.4$, and displaying only central jet breakup for $\theta = 0.6$. The higher thickness case, unlike the previous results, shows several discrepancies in terms of a standard trend. For $\theta = 0$, the jet breakup ranges from 1 to 3 times. For the following temperature, $\theta = 0.2$, there are no circumstances in which the jet breaks one time ($n_b = 1$). These results are in agreement with the

previous cases, in which the number of secondary droplets originated from the central jet breakup is promoted by higher values of θ. For the upper range, $\theta = 0.4$ and $\theta = 0.6$, the number of secondary droplets ranges between 3 and 5 with similar percentages, which is an increase when compared with lower temperatures. Therefore, both fuels have identical trends, as the rise in temperature promotes jet breakup and increases the number of secondary droplets originating from the central jet. The temperature increase is associated with the variation of the thermophysical properties of the fluids, which leads to lower values of surface tension and viscosity. The experimental results are in agreement with the literature [23,28], as higher Weber and lower Ohnesorge numbers promote jet breakup.

Figs. 14(a) and 14(b) display the central jet measurements of a water droplet impacting onto a heated liquid film for thicknesses of $h^* = 1.0$, and $h^* = 1.5$, respectively, where the temperature is varied between $0 \leq \theta \leq 0.6$. It is possible to observe that, for both cases,
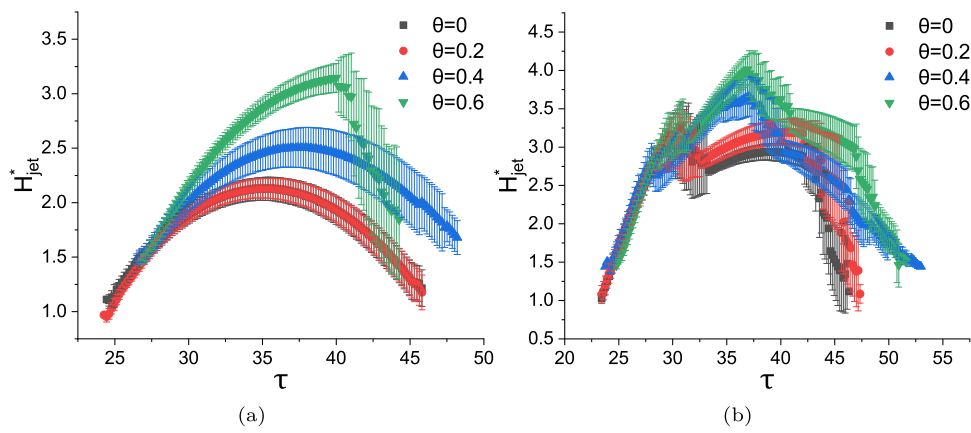
Fig. 9. Central jet height measurements of an n-heptane droplet impacting a liquid film for a range of dimensionless temperatures $(0 \leq \theta \leq 0.6)$: (a) $h^* = 1.0$; (b) $h^* = 1.5$.
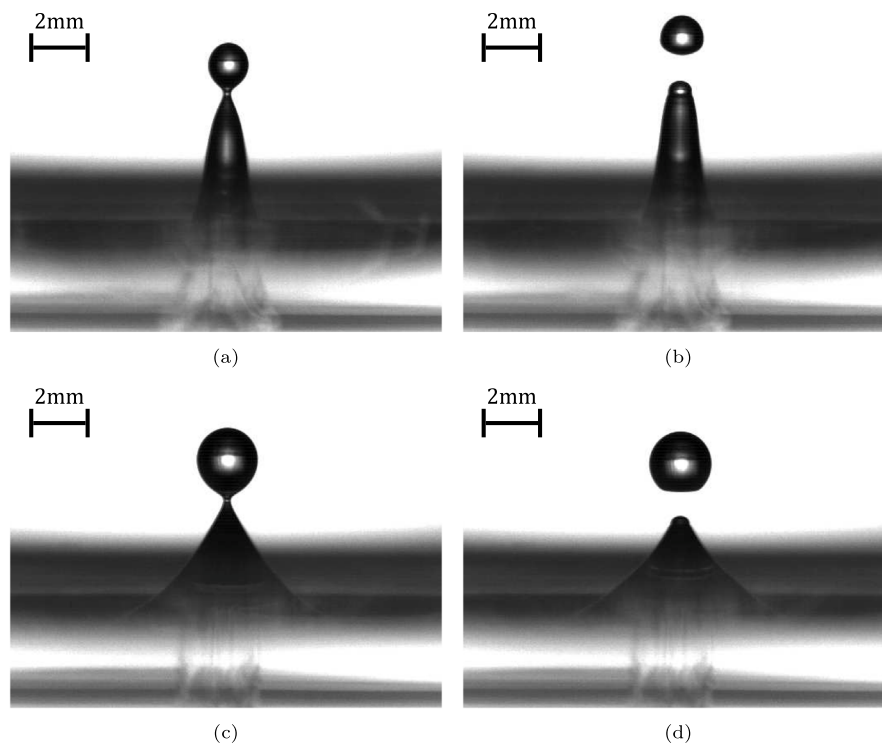

Fig. 10. Visualisation of central jet breakup subsequent to the impact of an n-heptane droplet $(\theta = 0, h^* = 1.5)$: (a) $\tau = 28.7$; (a) $\tau = 30.1$; (c) $\tau = 42.9$; (d) $\tau = 43.9$.
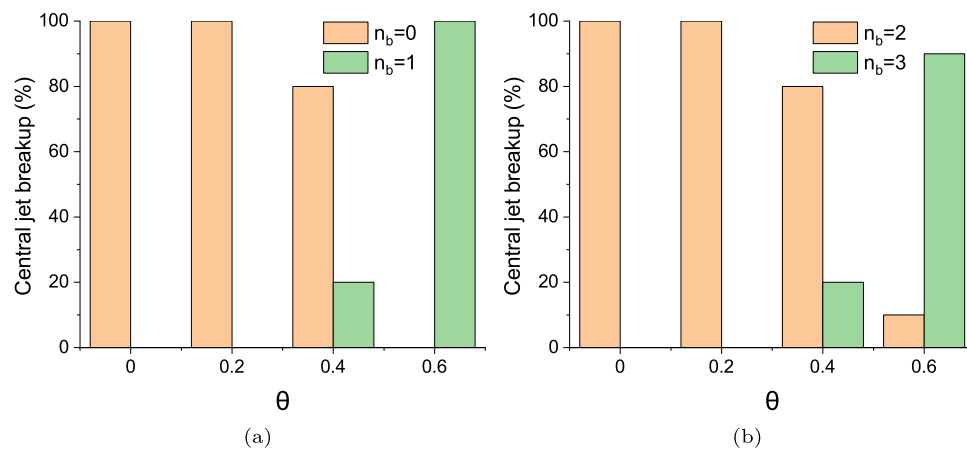

Fig. 11. Occurrence of central jet breakup of an n-heptane droplet impacting a liquid film for a range of dimensionless temperatures $(0 \leq \theta \leq 0.6)$, where n_b is the number of central jet breakups: (a) $h^* = 1.0$; (b) $h^* = 1.5$.
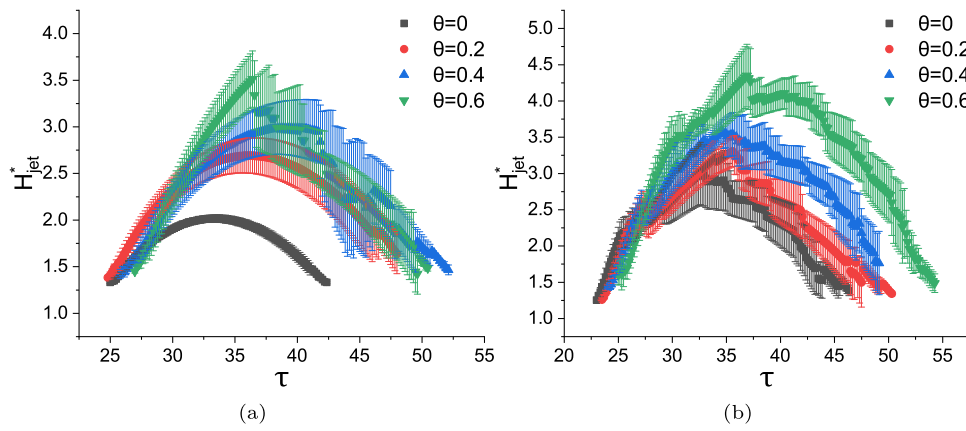
Fig. 12. Central jet height measurements of an n-decane droplet impacting a liquid film for a range of dimensionless temperatures ($0 \leq \theta \leq 0.6$): (a) $h^* = 1.0$; (b) $h^* = 1.5$.
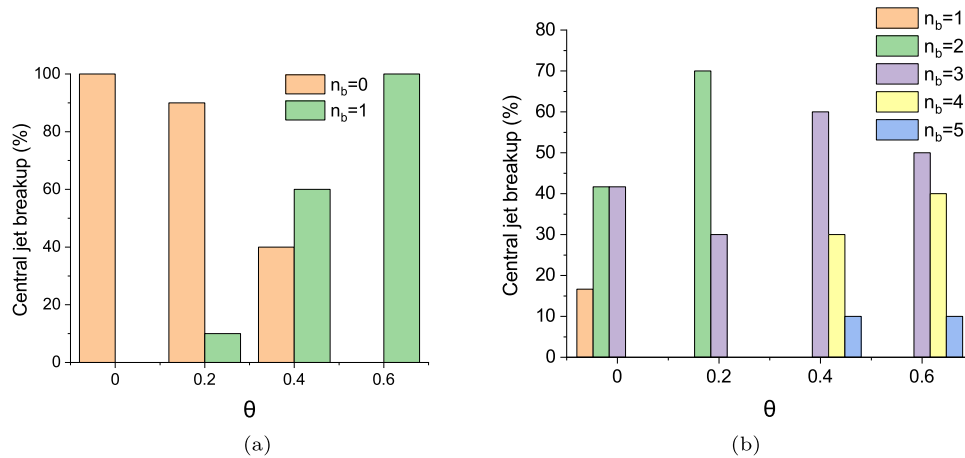

Fig. 13. Occurrence of central jet breakup of an n-decane droplet impacting a liquid film for a range of dimensionless temperatures ($0 \leq \theta \leq 0.6$), where n_b is the number of central jet breakups: (a) $h^* = 1.0$; (b) $h^* = 1.5$.
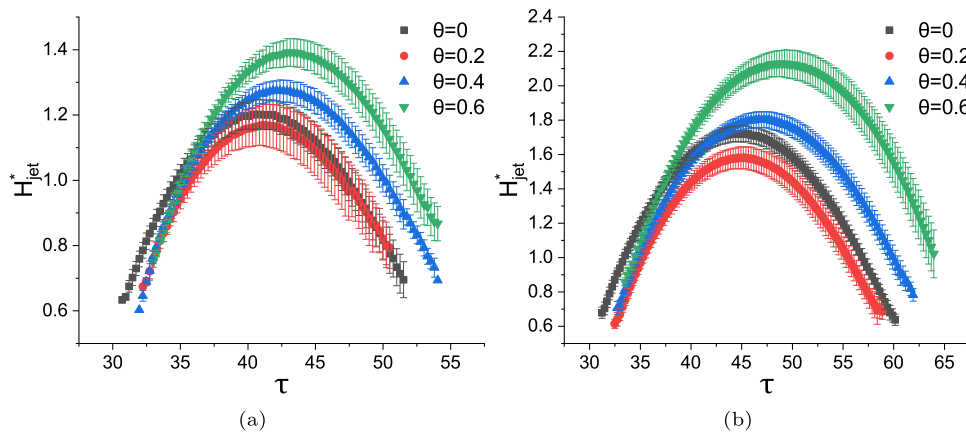

Fig. 14. Central jet height measurements of a water droplet impacting a liquid film for a range of dimensionless temperatures ($0 \leq \theta \leq 0.6$): (a) $h^* = 1.0$; (b) $h^* = 1.5$.

the maximum jet height occurs at later stages when increasing the film temperature. The central jet measurements display similar tendencies for the different conditions, in which the maximum height shows a reduction between $\theta = 0$ and $\theta = 0.2$, and a gradual increase for $\theta \geq 0.2$. With the exception of $\theta = 0.2$, the overall phenomenon duration increases with θ, which is also associated with reaching higher maximum jet height values. Central jet breakup is not visualised for the different conditions, as the curves follow a continuous path and do not display any discontinuities.

Overall, the increase of θ leading to higher central jet heights is associated with the differences in thermophysical properties due to temperature, such as lower values of viscosity and surface tension. This is also applicable to both n-decane and n-heptane. However, the unexpected reduction for $\theta = 0.2$ requires further studies to fully comprehend this regime. Therefore, in order to comprehend the deviation of the results regarding water for $\theta = 0.2$, a time scale analysis was performed. The time scales characteristic of the droplet impact phenomena for convection, surface tension, gravity, viscosity
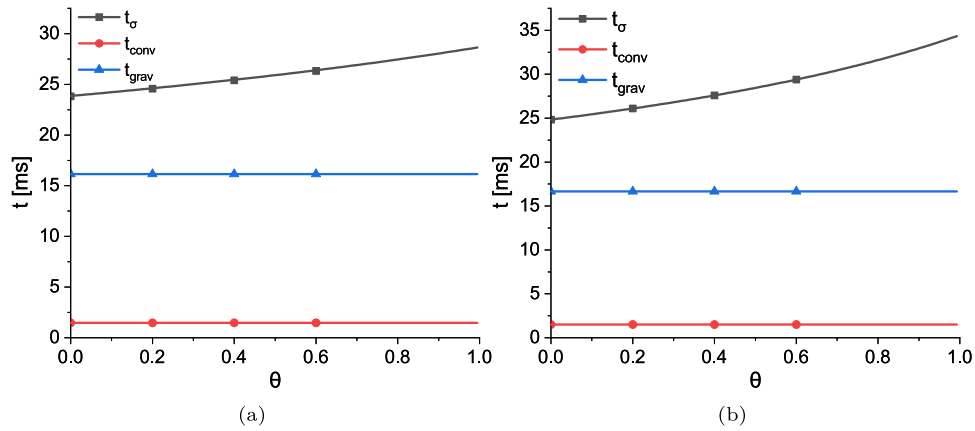
Fig. 15. Surface tension, convective and gravitational time scales as a function of θ for the droplet impact phenomenon: (a) N-heptane; (b) N-decane.
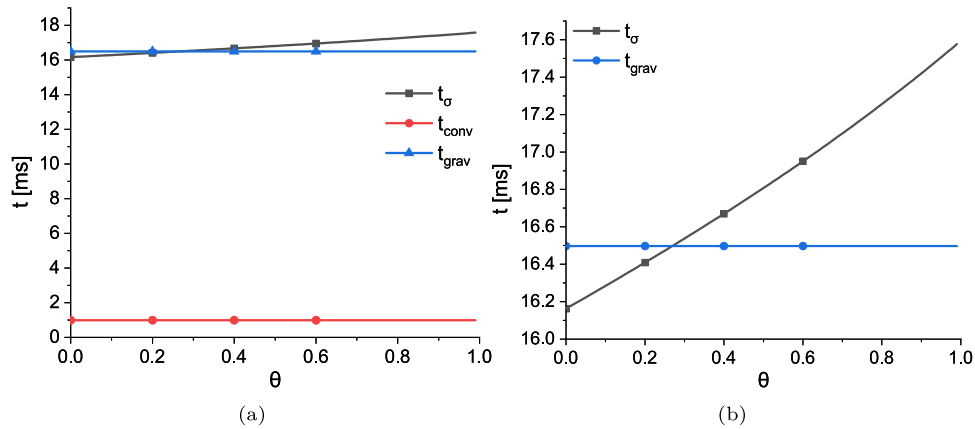

Fig. 16. Time scales as a function of θ for the water droplet impact: (a) Surface tension, convective and gravitational time scales; (b) Close-up of the surface tension and gravitational time scales.

and temperature [43] are defined by Eqs. (1)–(5), respectively:

$$t_{conv} = D_0/U_0 \tag{1}$$

$$t_{\sigma} = \left(\rho D_0^3/\sigma_f\right)^{1/2} \tag{2}$$

$$t_{grav} = \sqrt{D_0/g} \tag{3}$$

$$t_{vis} = D_0^2/\nu_f \tag{4}$$

$$t_{therm} = D_0^2/\alpha_f \tag{5}$$

where ν is the kinematic viscosity, α is the thermal diffusivity and the subscript f refers to the liquid film. The authors adapted the time scale equations by utilising the thermophysical properties of the liquid film rather than the droplet due to the influence of temperature on the phenomena.

Fig. 15 displays the convective, surface tension and gravitational time scales as a function of θ for the fuels. The viscous and thermal time scales are not displayed due to being 2 and 6 orders of magnitude higher than the closest time scale, respectively. Convection is a main factor in both fluids, as it is the lowest of all the scales, followed by the influence of the gravitational forces. These scales do not alter with θ due to their non-dependency on the liquid film thermophysical properties. However, the surface tension time scale depends on the density and surface tension, meaning that its value is affected by θ. Higher values of θ lead to an increase in the surface tension time scale, mostly due to the decrease of the surface tension (density also decreases, but

at a lower rate). In comparison with both gravitational and convective terms, the surface tension time scale has a lower influence on the overall phenomena. Therefore, the time scales can be represented by Eq. (6), which is applied for both conditions of n-heptane and n-decane.

$$t_{conv} < t_{grav} < t_{\sigma} \tag{6}$$

Fig. 16 performs a similar analysis to the previous case for the water droplet impact, where 16(a) displays the surface tension, convective and gravitational time scales as a function of θ, and 16(b) evidences the surface tension and gravitational scales in close detail. The convective forces are the predominant scale for the entirety of the temperature range. However, when comparing surface tension with gravitational time scales, the results differ quite significantly. For fuels, the gravitational has more influence than the surface tension time scale, $t_{grav} < t_{\sigma}$, regardless of temperature. For water, due to its high surface tension and variation with temperature, the gravitational and surface tension time scales intersect at approximately $\theta = 0.27$. For that reason, there is a region where the time scale associated with surface tension is predominant, which corresponds to $\theta < 0.27$, and a region where gravitational forces exceed surface tension, which is $\theta > 0.27$. Eq. (7) shows a bracket equation of the relation between the time scales for different domains of θ.

$$\begin{cases} t_{conv} < t_{\sigma} < t_{grav}, & \text{for } \theta < 0.27 \\ t_{conv} < t_{grav} < t_{\sigma}, & \text{for } \theta > 0.27 \end{cases} \tag{7}$$

When comparing the results between water and the fuels, it is possible to explain the distinctions at $\theta = 0.2$ based on the time scale analysis. Fuels show a clear difference between the order of magnitude

of the time scales, as represented by Eq. (6), whereas water has a shift between surface tension and gravitational time scales. This deviation, which occurs at $\theta = 0.27$, gives insight into the central jet height reduction at $\theta = 0.2$, which is followed by a constant increase of the jet height for higher values of θ. Therefore, water displays similar behaviour to fuels for $\theta > 0.27$, as the time scales follow the same relation for that specific temperature range, and a distinct behaviour for $\theta < 0.27$, as previously mentioned. Due to the quantitative results presented, both related to the central jet and to the time scales, a different approach to θ could be adapting the dimensionless numbers, such as the Weber and Reynolds Numbers, as a function of the liquid film thermophysical properties. This could give a distinct insight into how temperature affects the liquid film and subsequent impact phenomena, which could be considered for future works.

4. Conclusions and future work

The phenomena of droplet impact onto heated liquid films were studied for varying film temperatures and impact conditions, both qualitative and quantitatively. In terms of crater development, it is possible to visualise the formation of recirculation waves, predominant at the crater outer boundaries, which are promoted by the dimensionless temperature, θ. For water, the crater curvature is influenced by temperature, whereas for fuels, there is a shift in its shape, transitioning from an oblate to a conical shape. The central jet height measurements of the n-decane and n-heptane reveal that higher values of θ lead to an increase in the central jet height, as well as promoting and increasing the occurrence and number of secondary droplets originating from the central jet breakup, respectively. For water, no breakup was visualised, and the central jet height suffers a reduction between $\theta = 0$ and $\theta = 0.2$, which is not in agreement with the fuels. For $\theta = 0.4$ and $\theta = 0.6$, water follows a similar tendency to n-heptane and n-decane, displaying higher central jet values for increasing temperatures. The irregularities displayed for $\theta = 0.2$ can be explained by a time scale analysis, in which there is a shift in the regime between the surface tension and gravitational forces.

CRediT authorship contribution statement

Daniel A. Vasconcelos: Conceptualization, Methodology, Software, Validation, Formal analysis, Investigation, Data curation, Writing – original draft. **André R.R. Silva:** Resources, Writing – review & editing, Visualization, Supervision, Funding acquisition, Project administration. **Jorge M.M. Barata:** Resources, Writing – review & editing, Supervision, Funding acquisition.

Declaration of competing interest

The authors declare that they have no known competing financial interests or personal relationships that could have appeared to influence the work reported in this paper.

Data availability

Data will be made available on request.

Acknowledgements

Appendix. Physical properties

A.1. N-heptane

Density: $\rho = 0.23237 \times 0.26020^{-\left(1-(T/540.26)^{0.2791}\right)}$ [g/cm^3]

Viscosity: $log_{10}(\mu) = -5.7782 + 8.0587 \times 10^2/T + 1.3355 \times 10^{-2}T - 1.4794 \times 10^{-5}T^2$ [mPa s]

Surface tension: $\sigma = 53.64(1 - T/540.26)^{1.2431}$ [mN/m]

Thermal conductivity: $log_{10}(k) = -1.8482 + 1.1843(1 - T/536.40)^{2/7}$ [W/mK]

Heat capacity: $C_p = 101.121 + 9.7739 \times 10^{-1}T - 3.0712 \times 10^{-3}T^2 + 4.1844 \times 10^{-6}T^3$ [J/molK]

A.2. N-decane

Density: $\rho = 0.23276 \times 0.25240^{-\left(1-(T/618.45)^{0.28570}\right)}$ [g/cm^3]

Viscosity: $log_{10}(\mu) = -6.0716 + 1.0177 \times 10^3/T + 1.2247 \times 10^{-2}T - 1.1892 \times 10^{-5}T^2$ [mPa s]

Surface tension: $\sigma = 55.777(1 - T/618.45)^{1.3198}$ [mN/m]

Thermal conductivity: $log_{10}(k) = -1.7768 + 1.0839(1 - T/618.45)^{2/7}$ [W/mK]

Heat capacity: $C_p = 79.741 + 1.6926T - 4.5287 \times 10^{-3}T^2 + 4.9769 \times 10^{-6}T^3$ [J/molK]

References

[1] A.M. Worthington, A Study of Splashes, Longmans, Green, and Company, 1908.

[2] A.L. Yarin, et al., Drop impact dynamics: splashing, spreading, receding, bouncing, Annu. Rev. Fluid Mech. 38 (1) (2006) 159–192.

[3] C. Josserand, S.T. Thoroddsen, Drop impact on a solid surface, Annu. Rev. Fluid Mech. 48 (1) (2016) 365–391.

[4] G. Liang, I. Mudawar, Review of mass and momentum interactions during drop impact on a liquid film, Int. J. Heat Mass Transfer 101 (2016) 577–599.

[5] P. Foltyn, D. Ribeiro, A. Silva, G. Lamanna, B. Weigand, Influence of wetting behavior on the morphology of droplet impacts onto dry-patterned micro-structured surfaces, Phys. Fluids 34 (12) (2022) 123322.

[6] D.F. Ribeiro, A.R. Silva, M.R. Panão, Insights into single droplet impact models upon liquid films using alternative fuels for aero-engines, Appl. Sci. 10 (19) (2020) 6698.

[7] I. Ferrão, D. Vasconcelos, D. Ribeiro, A. Silva, J. Barata, A study of droplet deformation: The effect of crossflow velocity on jet fuel and biofuel droplets impinging onto a dry smooth surface, Fuel 279 (2020) 118321.

[8] G. Pacheco, A. Silva, M. Costa, Single-droplet combustion of jet a-1, hydroprocessed vegetable oil, and their blends in a drop-tube furnace, Energy & Fuels 35 (9) (2021) 7232–7241.

[9] I.A. Ferrao, A.R. Silva, A.S. Moita, M.A. Mendes, M.M. Costa, Combustion characteristics of a single droplet of hydroprocessed vegetable oil blended with aluminum nanoparticles in a drop tube furnace, Fuel 302 (2021) 121160.

[10] Š. Šikalo, E. Ganić, Phenomena of droplet–surface interactions, Exp. Therm Fluid Sci. 31 (2) (2006) 97–110.

[11] A. Moreira, A. Moita, M. Panao, Advances and challenges in explaining fuel spray impingement: How much of single droplet impact research is useful? Prog. Energy Combust. Sci. 36 (5) (2010) 554–580.

[12] R.P. Selvam, L. Lin, R. Ponnappan, Direct simulation of spray cooling: effect of vapor bubble growth and liquid droplet impact on heat transfer, Int. J. Heat Mass Transfer 49 (23–24) (2006) 4265–4278.

[13] D.B. van Dam, C. Le Clerc, Experimental study of the impact of an ink-jet printed droplet on a solid substrate, Phys. Fluids 16 (9) (2004) 3403–3414.

[14] R. Rioboo, C. Tropea, M. Marengo, Outcomes from a drop impact on solid surfaces, Atomization and Sprays 11 (2) (2001).

[15] A. Prosperetti, H.N. Oguz, The impact of drops on liquid surfaces and the underwater noise of rain, Annu. Rev. Fluid Mech. 25 (1993) 577–602.

[16] A. Bisighini, G.E. Cossali, C. Tropea, I.V. Roisman, Crater evolution after the impact of a drop onto a semi-infinite liquid target, Phys. Rev. E 82 (3) (2010) 036319.

[17] E. Berberović, N.P. van Hinsberg, S. Jakirlić, I.V. Roisman, C. Tropea, Drop impact onto a liquid layer of finite thickness: Dynamics of the cavity evolution, Phys. Rev. E 79 (3) (2009) 036306.

[18] X. Fan, C. Wang, X. Wang, M. Li, Z. Shen, Comparison of single droplet impact behaviors on the burning shallow/deep pool, Eur. J. Mech. B Fluids 74 (2019) 191–199.

[19] M. Xu, C. Wang, S. Lu, Water droplet impacting on burning or unburned liquid pool, Exp. Therm Fluid Sci. 85 (2017) 313–321.

[20] D. Kim, J. Lee, A. Bose, I. Kim, J. Lee, The impact of an oil droplet on an oil layer on water, J. Fluid Mech. 906 (2021).

[21] F. Minami, K. Hasegawa, Cavity and jet formation after immiscible droplet impact into deep water pool, Phys. Fluids 34 (3) (2022) 033315.

[22] X. Fan, C. Wang, F. Guo, B. Chen, M. Li, Water droplet impact on high-temperature peanut oil surface: The effects of droplet diameter and oil temperature, Int. J. Therm. Sci. 159 (2021) 106601.

[23] E. Castillo-Orozco, A. Davanlou, P.K. Choudhury, R. Kumar, Droplet impact on deep liquid pools: Rayleigh jet to formation of secondary droplets, Phys. Rev. E 92 (5) (2015) 053022.

[24] J. Eggers, E. Villermaux, Physics of liquid jets, Rep. Progr. Phys. 71 (3) (2008) 036601.

[25] S.J. Kim, S. Kim, S. Jung, Extremes of the pinch-off location and time in a liquid column by an accelerating solid sphere, Phys. Rev. Fluids 3 (8) (2018) 084001.

[26] H. Ma, C. Liu, X. Li, H. Huang, J. Dong, Deformation characteristics and energy conversion during droplet impact on a water surface, Phys. Fluids 31 (6) (2019) 062108.

[27] S.L. Manzello, J.C. Yang, An experimental study of a water droplet impinging on a liquid surface, Exp. Fluids 32 (5) (2002) 580–589.

[28] G.-J. Michon, C. Josserand, T. Séon, Jet dynamics post drop impact on a deep pool, Phys. Rev. Fluids 2 (2) (2017) 023601.

[29] E. Ghabache, A. Antkowiak, C. Josserand, T. Séon, On the physics of fizziness: How bubble bursting controls droplets ejection, Phys. Fluids 26 (12) (2014) 121701.

[30] R. Kumar, Lokesh, A.K. Das, Fluidics of an immiscible drop impact onto a hot oil film, Phys. Fluids 34 (1) (2022) 012108.

[31] M. Xu, C. Li, C. Wu, X. Chen, S. Lu, Regimes during single water droplet impacting on hot ethanol surface, Int. J. Heat Mass Transfer 116 (2018) 817–824.

[32] X. Yu, Y. Shao, K.-Y. Teh, D.L. Hung, Force of droplet impact on thin liquid films, Phys. Fluids 34 (4) (2022) 042111.

[33] N.E. Ersoy, M. Eslamian, Phenomenological study and comparison of droplet impact dynamics on a dry surface, thin liquid film, liquid film and shallow pool, Exp. Therm Fluid Sci. 112 (2020) 109977.

[34] İ. Dinçer, C. Zamfirescu, Drying Phenomena: Theory and Applications, John Wiley & Sons, 2016.

[35] S. Honnet, K. Seshadri, U. Niemann, N. Peters, A surrogate fuel for kerosene, Proc. Combust. Inst. 32 (1) (2009) 485–492.

[36] L. Zhao, T. Yang, R.I. Kaiser, T.P. Troy, M. Ahmed, D. Belisario-Lara, J.M. Ribeiro, A.M. Mebel, Combined experimental and computational study on the unimolecular decomposition of JP-8 jet fuel surrogates. I. n-Decane (n-C10H22), J. Phys. Chem. A 121 (6) (2017) 1261–1280.

[37] J. Farrell, N. Cernansky, F. Dryer, D.G. Friend, C. Hergart, C. Law, R. McDavid, C. Mueller, A. Patel, H. Pitsch, Development of an experimental database and kinetic models for surrogate diesel fuels, SAE Paper (2007–01) (2007) 0201.

[38] R. Lindstedt, L. Maurice, Detailed kinetic modelling of n-heptane combustion, Combust. Sci. Technol. 107 (4–6) (1995) 317–353.

[39] N. Otsu, A threshold selection method from gray-level histograms, IEEE Trans. Syst. Man Cybern. 9 (1) (1979) 62–66.

[40] M. H. Biroun, M. Rahmati, R. Tao, H. Torun, M. Jangi, Y. Fu, Dynamic behavior of droplet impact on inclined surfaces with acoustic waves, Langmuir 36 (34) (2020) 10175–10186.

[41] B.R. Mitchell, J.C. Klewicki, Y.P. Korkolis, B.L. Kinsey, The transient force profile of low-speed droplet impact: measurements and model, J. Fluid Mech. 867 (2019) 300–322.

[42] D.F. Ribeiro, M.R. Panão, J.M. Barata, A.R. Silva, Insights on bubble encapsulation after drop impact on thin liquid films, Int. J. Multiph. Flow. (2023) 104450.

[43] M. Rein, Drop-Surface Interactions, (456) Springer Science & Business Media, 2002.